Cascade of pressure-driven phase transitions in the topological nodal-line superconductor PbTaSe2

Tahir Murtaza, Haiyang Yang, Jiajia Feng, Yi Shen, et.al.

Published version information

Citation: T Murtaza et al. Cascade of pressure-driven phase transitions in the topological nodal-line superconductor PbTaSe2. Phys Rev B 106, no. 6 (2022): L060501.

DOI: 10.1103/PhysRevB.106.L060501

Letter

Cascade of pressure-driven phase transitions in the topological nodal-line superconductor $PbTaSe_2$

Tahir Murtaza,[1,2] Haiyang Yang,[3] Jiajia Feng,[4] Yi Shen,[5] Yongheng Ge,[5] Yi Liu,[1] Chunqiang Xu,[1,4] Wenhe Jiao,[1] Yaokang Lv,[6] Christopher J. Ridley,[7] Craig L. Bull,[7,8] Pabitra K. Biswas,[7] Raman Sankar,[9] Wei Zhou,[10] Bin Qian,[10] Xuefan Jiang,[10] Zhenjie Feng,[11] Yonghui Zhou,[3] Ziming Zhu,[5,*] Zhaorong Yang,[3,†] and Xiaofeng Xu[1,‡]

[1]*Key Laboratory of Quantum Precision Measurement of Zhejiang Province, Department of Applied Physics, Zhejiang University of Technology, Hangzhou 310023, China*

[2]*College of Information Engineering, Zhejiang University of Technology, Hangzhou 310023, China*

[3]*Anhui Province Key Laboratory of Condensed Matter Physics at Extreme Conditions, High Magnetic Field Laboratory, Chinese Academy of Sciences, Hefei 10 230031, China*

[4]*School of Physics and Key Laboratory of MEMS of the Ministry of Education, Southeast University, Nanjing 211189, China*

[5]*Key Laboratory of Low-Dimensional Quantum Structures and Quantum Control of Ministry of Education, Department of Physics and Synergetic Innovation Center for Quantum Effects and Applications, Hunan Normal University, Changsha 410081, China*

[6]*College of Chemical Engineering, Zhejiang University of Technology, Hangzhou 310014, China*

[7]*ISIS Pulsed Neutron and Muon Source, STFC Rutherford Appleton Laboratory, Harwell Campus, Didcot, Oxfordshire OX11 0QX, United Kingdom*

[8]*School of Chemistry, University of Edinburgh, David Brewster Road, Edinburgh EH9 3FJ, United Kingdom*

[9]*Institute of Physics, Academia Sinica, Nankang, Taipei 11529, Taiwan*

[10]*Department of Physics, Changshu Institute of Technology, Changshu 215500, China*

[11]*Materials Genome Institute, Shanghai University, Shanghai 200444, China*

(Received 27 May 2022; revised 3 July 2022; accepted 22 July 2022; published 2 August 2022)

We report a succession of pressure-tuned structural transitions in the topological nodal-line superconductor $PbTaSe_2$, evidenced from synchrotron x-ray diffraction, elastic neutron scattering, Raman spectroscopy, and electrical transport measurements up to 56 GPa, accompanied by first-principles calculations to uncover the evolution of the underlying electronic structure. In contrast to the previously proposed small shift of the Pb Wyckoff coordinate in the sub-GPa regime, our study reveals that it is rather a transition from $P\bar{6}m2$ (α phase) to $P6_3mc$ (β phase), subsequently followed by a transition to $P6/mmm$ (γ phase) at ~7.5 GPa and to $Pmmm$ (δ phase) at ~44 GPa. In addition, the first-principles calculations unambiguously demonstrate the multiple types of topological fermions associated with these different pressure-driven structures. Collectively, our results not only present the intriguing structural transitions in this topological $PbTaSe_2$ superconductor, they also provide the impetus to study topological phase transitions and their physical consequences in a broader class of topological materials.

DOI: 10.1103/PhysRevB.106.L060501

Topological semimetals, such as Dirac, Weyl, and nodal-line semimetals, have been a subject of intense interest ever since they were theoretically predicted and experimentally verified, revitalizing the field of condensed-matter physics [1–5]. Apart from their conceptual richness, topological semimetals also hold promise for applications in, for instance, spintronics, based on their spin-momentum-locked surface states. Despite many nodal-line semimetals having been theoretically proposed, only some of them, such as $ZrSiX$ (X = S, Se, Te) [6,7], $PbTaSe_2$ [8–13], $AuSn_4$ [14], $SrAs_3$ [15], and MnAlGe [16], have been synthesized and validated in experiments. Among these nodal-line semimetals, some have been found to be superconducting at ambient conditions and as such, they provide the material candidates in studying topological superconductivity. $PbTaSe_2$ is such an example.

Although it was first discovered in the 1980s [8], $PbTaSe_2$ only attracted tremendous research interest in recent years after its topological electronic structure was experimentally identified [9–13,17,18]. This stoichiometric $PbTaSe_2$ is particularly interesting as it is also superconducting below T_c = 3.8 K at ambient pressure, offering an interesting playground to study topological superconductivity [9,10,18,19]. Structurally, $PbTaSe_2$ consists of alternating stacks of hexagonal $TaSe_2$ and Pb layers, with the Ta atoms situated at a position that breaks the inversion symmetry [see Fig. 1(a)]. This crystal structure has the $P\bar{6}m2$ space group. Due to its noncentrosymmetric structure and strong spin-orbit coupling (SOC) inherent to the heavy Pb atom, the spin degeneracy of electronic bands is lifted and lines of Dirac nodes are formed in the vicinity of the Fermi level [10]. The bulk superconductivity observed in this Dirac nodal-line semimetal makes it one of the candidates to host topological superconductivity

*zimingzhu@hunnu.edu.cn
†zryang@issp.ac.cn
‡xuxiaofeng@zjut.edu.cn

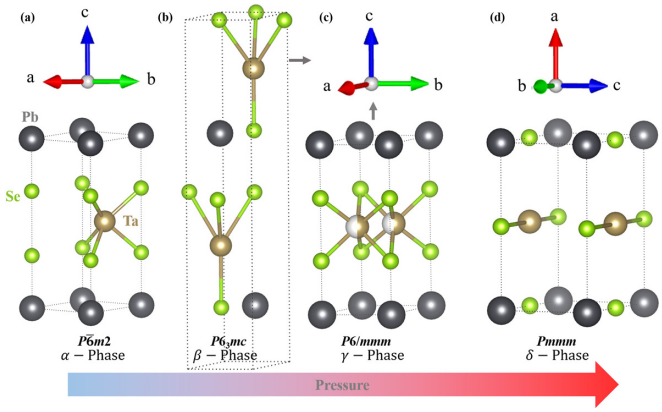

FIG. 1. Schematic diagrams of the crystal structure evolution with increasing pressure. There exist four different structures up to 56 GPa, with space groups of $P\bar{6}m2$, $P6_3mc$, $P6/mmm$, and $Pmmm$ that are denoted as the α phase, β phase, γ phase, and δ phase, respectively. Note that the c-axis lattice constant is nearly doubled in the β phase. In the γ phase, the half-white–half-gold sphere indicates Ta positions are only half occupied.

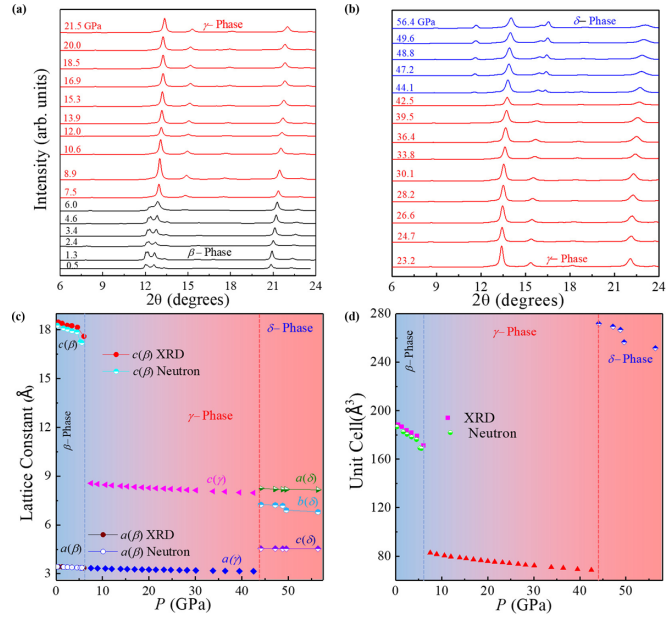

FIG. 2. The XRD patterns under pressure and the extracted lattice parameters. (a) and (b) The XRD patterns of $PbTaSe_2$ taken in a pressure range of 0.5–56.4 GPa. From a pressure of ∼0.5 to ∼6 GPa, it is the β phase; from ∼7.5 to ∼42.5 GPa, it is the γ phase; from ∼44.1 to ∼56.4 GPa, it is the δ phase. For clarity, the index for each peak is only illustrated in the first panel of Figs. S3– S5 in the SM for each phase [23]. (c) and (d) The lattice constants and the unit-cell volumes in individual phases.

[10,18]. Indeed, topological surface states have recently been visualized by scanning tunneling microscopy and the Majorana bound states were also claimed on the Pb-terminated surface of this fully gapped superconductor [18].

More intriguingly, it was recently observed that the structure of $PbTaSe_2$ is highly sensitive to external pressure [20–22]. A sharp, first-order structural transition (occurring at ambient pressure near ∼425 K) was found to be entirely suppressed by a small hydrostatic pressure of ∼0.25 GPa, accompanied by a steplike decrease of T_c in the new phase [see Fig. S6 in the Supplemental Material (SM) for the low-pressure phase diagram [23]]. In this new structure, the c-axis lattice parameter shrinks (more precisely, $c/2$ in the new structure is smaller than c of the pristine $P\bar{6}m2$ phase if the unit cell is nearly doubled along the c axis, as it occurs here, to be discussed later) whereas the a axis expands [21]. Although the first-principles calculations suggested that this is due to the shift of Pb atoms from the 1a to 1e Wyckoff position with Ta and Se positions remaining unchanged [21], direct experimental evidence for this structural transition is still lacking.

Here, we report a synchrotron x-ray diffraction (XRD) study of the crystal structure of $PbTaSe_2$ up to 56 GPa to reveal the nature of its structural transitions under pressure. In contrast to a previous proposal [21], it is found that the lattice actually undergoes a transition from $P\bar{6}m2$ (α phase) to $P6_3mc$ (β phase) in the sub-GPa pressure regime. In addition, there are two more structural transitions in the high-pressure range, driving the lattice to $P6/mmm$ (γ phase) at ∼7.5 GPa and to $Pmmm$ (δ phase) at ∼44 GPa, sequentially. Complementary to the synchrotron XRD, elastic neutron scattering, Raman spectroscopy, and electrical transport have also been conducted to investigate the change in its electronic and lattice properties. Importantly, the electronic band structure, studied by first-principles calculations, displays a plethora of topologically nontrivial states rooted in these structures, providing a versatile platform to study topological phase transitions under pressure.

The experimental and computational methods used in this study as well as some supporting data under pressure are described in the SM [23–33]. The powder XRD pattern of the pulverized $PbTaSe_2$ single crystals at ambient pressure and temperature has been studied and it is found that the diffraction peaks of our samples can be indexed into the noncentrosymmetric $P\bar{6}m2$ space group (No. 187), consistent with previous works [17]. The lattice constants extracted from XRD are $a = 3.45$ Å and $c = 9.35$ Å. This structure is comprised of alternately stacked hexagonal Pb and $TaSe_2$ layers [Fig. 1(a)]. In the $TaSe_2$ layer, a hexagonal Ta atomic plane is sandwiched by two hexagonal Se atomic layers. The lattice can thus be viewed as a Pb layer intercalating two adjacent $TaSe_2$ layers with Pb atoms sitting right above the Se atoms. Further, we performed the high-pressure synchrotron XRD measurements on the pulverized single crystals as shown in Fig. 2 at different pressures. The data were taken in the angle range of $2\theta = 6°$–$24°$ and the Le Bail refinement was utilized to identify the underlying phases. Note that this angle range is very limited due to the intrinsic technical issue in all high-pressure XRD experiments with the diamond anvil cell. It is found that the data between 0.5 and 6 GPa cannot be indexed with $P\bar{6}m2$, nor to the Pb-1e (Pb-1c) structure suggested by Kaluarachchi *et al.* [21], where the Pb atom shifts from the 1a to 1e (1c) Wyckoff positions without changing the global symmetry. Rather, the data can only be overall fitted with the $P6_3mc$ space group that was also considered in their pioneering work [21]. The $P6_3mc$ structure can be obtained by doubling the unit cell of the $P\bar{6}m2$ structure along the c-axis lattice vector and then moving the upper half of the unit cell

by 1/3 along the long diagonal of the basal plane [$1/3(b-a)$] [see Fig. 1(b) and Ref. [21]]. This $P6_3mc$ structure under this low pressure can be well justified for the following reasons: As indicated by transmission electron microscopy (TEM) and XRD measurements at ambient pressure [21], compared to the $P\bar{6}m2$ phase, this high-temperature/high-pressure phase shows a contraction in the c-axis constant (or more precisely, $c/2$ of the new phase is smaller than c of the original $P\bar{6}m2$ phase if the unit cell is doubled along the c axis, as it occurs here) while the basal plane (a axis) undergoes a normal expansion. Our fitting at 0.5 GPa also shows this trend; $c/2$ in the $P6_3mc$ phase is smaller than the c-axis lattice constant of the $P\bar{6}m2$ phase whereas the a axis gets expanded.

As the pressure is further increased beyond 6.0 GPa, new peaks emerge in the XRD pattern, suggestive of the new structural transition. The pattern at 7.5 GPa can be best fitted with the $P6/mmm$ space group (hexagonal), in which Ta atoms sit at one of two equivalent (1/3, 2/3, 1/2) sites with half occupancy, i.e., Ta is distributed evenly statistically without ordering within each $TaSe_2$ layer [Fig. 1(c)]. As seen from Fig. 2, this same structure persists up to ∼42.5 GPa. In this $P6/mmm$ structure, the unit cell is comprised of alternately stacked hexagonal Pb and $TaSe_2$ layers. In the $TaSe_2$ layers, a hexagonal Ta atomic plane is sandwiched between two hexagonal Se atomic planes, and the Pb atomic layer is intercalated between two adjacent $TaSe_2$ layers, with Pb atoms sitting right above the Se atoms [see Fig. 1(c)]. In this structure, Pb occupies the Wyckoff $1a$ position and Ta (Se) resides at the position of $2d(2e)$. A further increase in the pressure causes the splitting of a peak around $2\theta \sim 16^\circ$ and an additional peak around 11° [Fig. 2(b)]. The XRD patterns from 44.1 to 56.4 GPa have been fitted with the $Pmmm$ (orthorhombic) space group as demonstrated in the SM (Fig. S5) [23]. In this unit cell, Pb is located at the orthorhombic corners; Ta and Se coordinates are schematically shown in Fig. 1(d). Here, Pb is at the Wyckoff position of $1a$ and Ta (Se) at the position of $1f$ ($1b$ and $1e$).

The lattice parameters and the volume of the unit cell extracted from the above XRD analysis are summarized in Fig. 2. For simplicity, we designate the space groups $P\bar{6}m2$, $P6_3mc$, $P6/mmm$, and $Pmmm$ as the α, β, γ, and δ phases, respectively. The lattice parameters are denoted as, e.g., $a(\beta)$ and $c(\beta)$ for the β phase and likewise for others. The phase-wise variation of lattice parameters with pressure is depicted in Fig. 2. In the β phase, the c-axis lattice parameter is nearly doubled compared with that of the α phase, while in the γ phase, it is halved again. In parallel, the structure in the pressure range of 0.06–5.58 GPa has also been studied by neutron diffraction at room temperature and the data were fitted by the Rietveld refinement using the FULLPROF program (see SM [23]). As noted, the structure at 0.06 GPa belongs to the α phase with the lattice parameters $a = 3.43$ Å and $c = 9.38$ Å, comparable to those extracted at ambient pressure. Similar to the XRD study, the structure in the pressure range of 0.26–5.58 GPa belongs to the β phase. The neutron diffractions at 0.06 GPa (α phase) and 0.26 GPa (β phase) fitted with the Rietveld refinement are shown in the SM [23]. The variation of lattice parameters and the unit-cell volume achieved from the neutron analysis is also incorporated in Fig. 2 and seen to follow the same trend as those observed from the XRD.

The unit-cell volume for these four phases shows an interesting pressure dependence [Fig. 2(d)]. The volume of the β phase is observed to decrease with increasing pressure and gets almost halved once reaching the γ phase. The γ phase then shows a monotonic decrease in volume as the pressure increases further. Upon reaching the orthorhombic δ phase, the unit-cell volume shows an abrupt expansion and it get compressed again with a further increase in pressure.

Raman spectroscopy is a technique that is widely used to determine the nature of bonds and their vibrations and is thereby a useful tool in high-pressure studies [34–37]. Here, we studied the Raman spectrum of $PbTaSe_2$ under high pressure up to ∼50 GPa. As known, in high temperatures, a $2H$-$TaSe_2$ crystal structure possesses hexagonal D^4_{6h} (space group $P6_3/mmc$) symmetry and the irreducible representation of Raman active modes is given by $\Gamma = A_{1g} + 2E_{2g} + E_{1g}$ [38]. Recently, Glamazda *et al.* doped Pb in $TaSe_2$ and studied the Raman spectrum of Pb_xTaSe_2 [39] and proposed three space groups $P\bar{6}m2(D_{3h})$, $P6(C_6)$, and $P6_3/mmc(D_{6h})$ for its structure at ambient conditions (zero pressure and room temperature). The trigonal crystal structure D_{3h} (space group $P\bar{6}m2$), being the most plausible structure under ambient conditions, yields $\Gamma = A' + 3E' + E''$ Raman active modes. The A', E', and E'' are correlated to A_{1g}, E_{2g}, and E_{1g} modes of $2H$-$TaSe_2$, respectively. The additional mode with E' symmetry has been assigned to the existence of a Pb atom in the system [39,40]. We have observed a structural transition by the application of pressure at 0.5 GPa from the XRD studies and the structure in the pressure range of 0.5–6.0 GPa has been fitted with the $P6_3mc$ (C_{6v}) space group. The group-theoretical symmetry analysis yields the irreducible representations of the Γ-point phonon Raman modes for such a system as follows: $\Gamma = 3A_1 + 4E_2 + 3E_1$ [41]. The structural phase transition occurring at 7.5 GPa possesses a $P6/mmm(D_{6h})$ space group as observed from the XRD analysis and the Raman modes for such a system are given as $\Gamma = A_{1g} + E_{2g} + E_{1g}$ [39]. The next structural phase transition occurring at 44.1 GPa possesses an orthorhombic phase with the space group $Pmmm$ and does not possess any Raman mode [41], as seen from Fig. 3(b). The pressure-dependent Raman spectra ranging from 0.96 to 49.5 GPa is encapsulated in Figs. 3(a) and 3(b).

The phonon mode $M1$ appearing at a frequency of 232 cm^{-1} existing at pressure 0.96 GPa corresponds to the E^1_{2g} mode [39]. The increase in the pressure causes the peak to shift to a lower wave number. The compression in general causes the phonon modes to shift to a higher wave number due to the decrease in the length of bonds that possess the vibrations. However, the mode frequency may decrease sometimes due to the applied pressure, and such modes are known as soft modes. The reason for softening of the Raman modes on the application of pressure may be attributed to the decrease in bond strength [42]. Mishra *et al.* have also observed a similar shift in the pressure-dependent Raman mode existing at 557 cm^{-1} in a TiS_3 system [43]. Similarly, the Raman spectra of $GaTa_4Se_8$ measured at room temperature up to a pressure of 15 GPa showing the dominant mode at 236 cm^{-1} has also shown softening [44]. One can infer the crystal instability from the presence of such soft modes in a system when it goes through a structural phase transition. The XRD studies

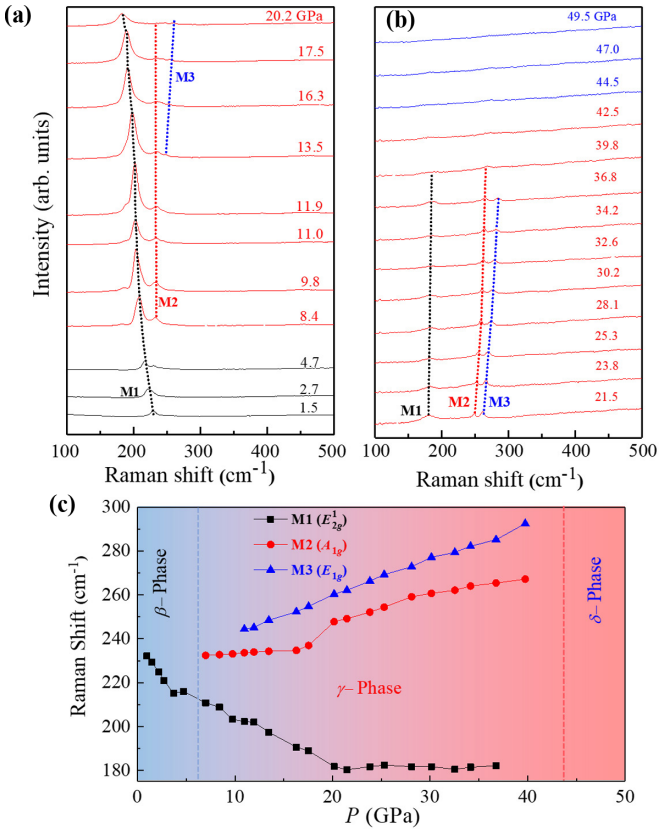

FIG. 3. Raman spectroscopy under pressure. (a) and (b) The Raman spectra of $PbTaSe_2$ under pressure up to 50 GPa. (c) The Raman modes plotted as a function of applied pressure.

show a decrease in the value of the lattice parameters as we increase the pressure beyond 0.5 GPa. The decrease in the lattice parameters causes the $M1$ to shift to the lower wave number. At a pressure of 7 GPa, there appears another peak $M2$ at 228 cm^{-1}, corresponding to the A_{1g} mode that shifts to a higher wave number on increasing pressure and sustains up to the pressure of 39.8 GPa. The third peak $M3$ appearing at 244 cm^{-1} corresponds to the E_{1g} phonon mode which appears beyond the pressure of 11 GPa. The shift of Raman modes with pressure is summarized in Fig. 3. The observed phonon modes are consistent with the factor group prediction for the $P6/mmm$ space group. From a pressure of 44.1 GPa onwards, the structure turns to the orthorhombic phase and the Raman peaks diminish altogether. Since the pressure causes geometric changes in the structure of $PbTaSe_2$ as evidenced from the XRD study, the Raman modes also show changes with the variation of applied pressure.

The resistivity was seen to be monotonically suppressed by pressure up to 51 GPa, as illustrated in the SM [23]. No superconductivity was observable above 1.1 GPa (β phase) down to 2 K. As discussed in Refs. [45,46], the superconductivity in $PbTaSe_2$ is intimately related to the strong electron-phonon coupling associated with the A_{1g} phonon mode at the momentum L. The origin for the disappearance of superconductivity in the γ phase and δ phase at high pressure is unknown to us. It may be linked to the stiffening of the A_{1g} phonon under pressure, as revealed in the Raman study.

In order to better understand the topological properties of all phases revealed above, we calculated the band structures for these four phases using first-principles calculations. In the γ phase, however, only one of two Ta positions is evenly occupied, which makes the calculation difficult. Here, we calculated the band structure with Ta positions fully occupied and *a priori* assume that the half occupancy of Ta only shifts the Fermi level compared to the fully occupied phase. As shown in Fig. 4, all phases exhibit metallic characteristics, which in fact feature a different band topology. Here, experimental lattice constants are adopted for all the structures and spin-orbit coupling is considered in our calculations. Note that the inversion symmetry (P) is broken for α and β phases, while P is preserved for γ and δ phases. Time-reversal symmetry (T) is respected for all of them since they do not contain any magnetic atoms. The additional symmetrical operators for the symmetry analysis are a horizontal mirror symmetry M_z for the α phase, three vertical (glide) mirror symmetries $\widetilde{M}_{x\bar{y}} = M_{x\bar{y}}|00\frac{1}{2}\}$, $\widetilde{M}_{2xy} = M_{2xy}|00\frac{1}{2}\}$, and M_y, and twofold screw rotation along z, $S_{2z} = \{C_{2z}|00\frac{1}{2}\}$ for the β phase, and threefold rotation along the z axis (C_{3z}) and mirror symmetry M_x for the γ phase. Here, $M_{x\bar{y}} : (x, y, z) \rightarrow (y, x, z)$ and $M_{2xy} : (x, y, z) \rightarrow (-x, -x + y, z)$.

Let us start from the α phase. One can observe that two bands cross each other near the Fermi level, which form two nodal lines located on the plane of $k_z = \pi/c_\alpha$ (where c_α is the c lattice constant for the α phase, etc.), as shown in Fig. 4(g). Through first-principles calculations, we find that the crossed bands host opposite mirror eigenvalues ($+i$ or $-i$), demonstrating that the nodal lines are protected by M_z. These results are consistent with previous work [10]. Intriguingly, for the β phase, the calculated band structure demonstrates there exist multiple types of band crossings, including type-II Weyl nodal lines, type-II Dirac points, and a twofold nodal surface, in the vicinity of the Fermi level as plotted in Figs. 4(c)– 4(f) and 4(h). Remarkably, there exists a pair of Dirac points along the A-L direction, which is protected by M_y and the combination of S_{2z} and T [47] [see Figs. 4(c) and 4(h)]. In reality, there is a twofold nodal surface located on the plane of $k_z = \pi/c_\beta$ as a protection of S_{2z} and T [47,48] [see Figs. 4(f) and 4(h)]. In addition, one can see that four type-II Weyl nodal lines traverse the whole BZ, in which NL_1 and NL_2 are protected by M_y and they eventually meet at the position of the Dirac points [see Figs. 4(c) and 4(h)], and NL_3 and NL_4 are protected by $\widetilde{M}_{x\bar{y}}$ and $\widetilde{M}_{2xy}$ [see Figs. 4(d) and 4(e)], respectively. In Fig. 4(i), we plot the results of the band structure for the γ phase when two Ta positions are fully occupied, i.e., the $PbTa_2Se_2$ phase. It is clear that there is a pair of Dirac points formed by two bands with the double irreducible representations of Γ_7 and Γ_9 along the K-H direction, which is guaranteed by P, T, M_x, and C_{3z} [49,50]. Furthermore, based on the Fu-Kane formula from Ref. [51], the Z_2 invariant for the plane of $k_z = 0$ can be evaluated from the parities of the occupied bands, and we find Z_2 $(k_z = 0) = 1$ for the γ phase. Lastly, the bulk band structure of the δ phase is illustrated in Fig. 4(j). Band inversion occurs around the Z point, implying that this system possesses a nontrivial topology. Indeed, by using the Fu-Kane formula [51], it is also revealed that the δ phase stays in the strong topological regime, for which the topological indices are $(\nu_0; \nu_1\nu_2\nu_3) = (1; 001)$.

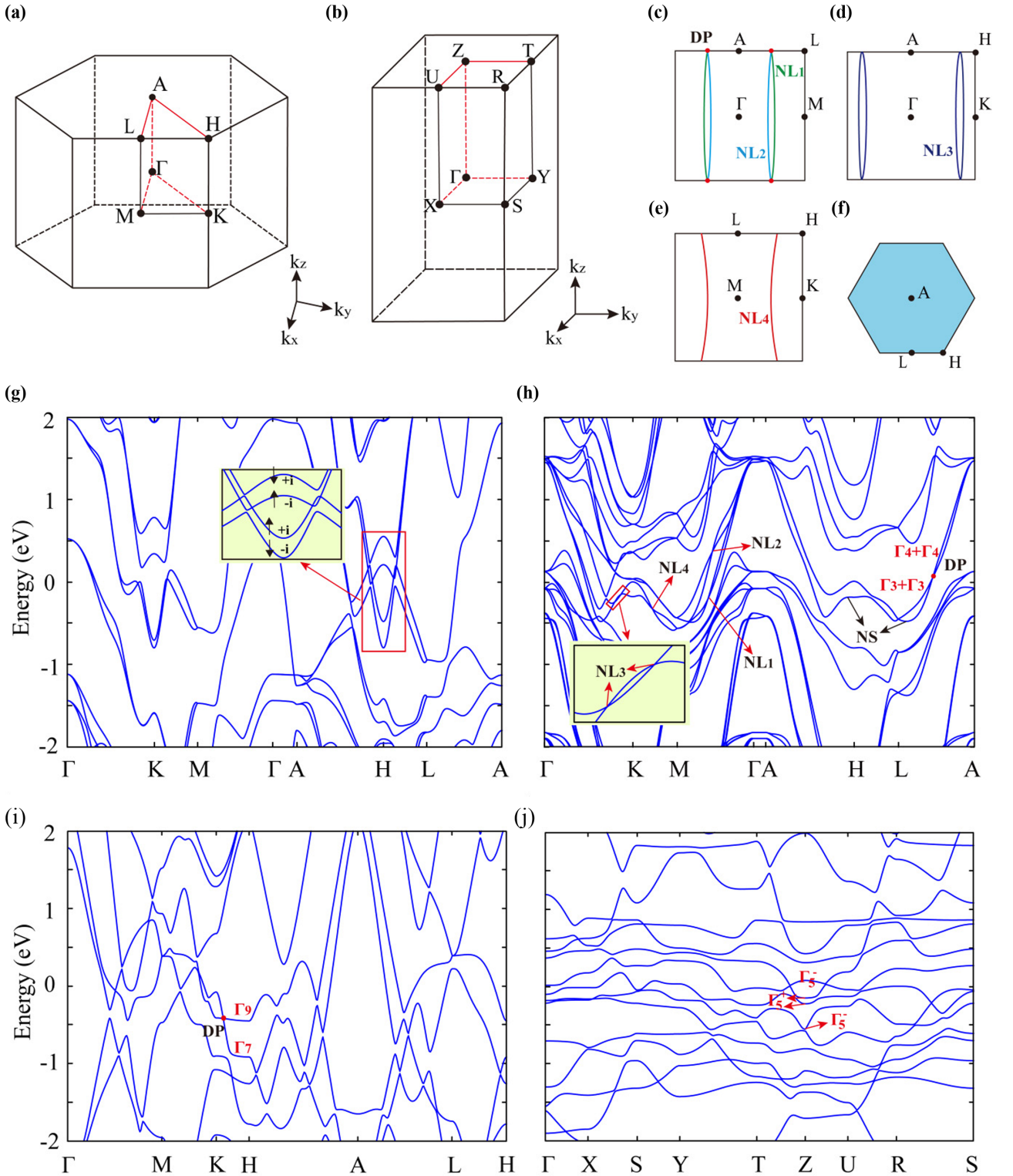

FIG. 4. The electronic structure of individual phases. (a) Bulk BZ for the α, β, and γ phases, and (b) bulk BZ for the δ phase. Here, black dots indicate the high-symmetry points. Bulk band structures for (g) α, (h) β, (i) γ, and (j) δ phases. $\pm i$ indicates the calculated mirror eigenvalues for the bands around the H point. Red dots indicate Dirac points along the A-L direction for the β phase and the K-H direction for the γ phase. Black arrows indicate the nodal surface (NS) in (h). (c)–(e) show four type-II nodal lines on the distinct planes, respectively. (f) The distribution of the nodal surface on the plane of $k_z = \pi/c_\beta$.

To summarize, by means of synchrotron x-ray diffraction up to 56 GPa, we are able to identify a series of pressure-induced structural transitions in the archetypal topological superconductor candidate $PbTaSe_2$. Contrary to the previous thought that only a small change of Wyckoff coordinate occurs in the sub-GPa regime, our study instead revealed a structural transition that doubles the c-axis lattice, giving rise to a significant modification in the electronic structure, characterized by multiple band crossings that form an isolated Dirac node, Dirac nodal line, and Dirac nodal surface. The structural transitions at higher pressure lead to other distinct topological phases, thereby making it a different platform to study the topological phase transitions in a stoichiometric material. The structural transition was further studied by Raman scattering that reveals the associated lattice deformation and phonon modes. The electrical resistivity was seen to be progressively suppressed by the pressure with no signature of quantum criticality [52] and no superconductivity can be observed above $\sim$2 GPa. It was suggested that the superconductivity of $PbTaSe_2$ arises from the drastically enhanced electron-phonon coupling associated with the A_{1g} phonon mode [45,46]. The absence of superconductivity under high pressure, therefore, may be related to a significant shift of the A_{1g} phonon mode under pressure as revealed in the Raman study. Overall, our results establish that $PbTaSe_2$ is an interesting material for investigating the interplay between structure and topology, and potentially a plethora of topologically nontrivial phases rooted in this interplay.

The authors would like to thank Nigel Hussey, Michael Smidman, Xin Lu, Yu Song, Dong Qian, Xiangang Wan, and Bin Li for valuable discussions, and thank Xiaolong Li for the technical support. This research was supported by National Natural Science Foundation of China under Grants No. 11974061 and No. U1832147. The synchrotron XRD under pressure was performed in the Beamline BL15U1 of the Shanghai Synchrotron Radiation Facility (SSRF). R.S. acknowledges the financial support provided by the Ministry of Science and Technology (MOST), Taiwan, under Grants No. MOST-110-2112-M-001-065-MY3 and No. 111WIA0110339 and Academia Sinica for the budget of AS-iMATE-19-111. Z.Z. was supported by the National Natural Science Foundation of China (Grant No. 11704117), the Hunan Provincial Natural Science Foundation of China (Grant No. 2022JJ30370), and the Project of Educational Commission of Hunan Province of China (Grant No. 21A0066).

T.M., H.Y., and J.F. contributed equally to this work.

[1] M. Z. Hasan and C. L. Kane, Rev. Mod. Phys. **82**, 3045 (2010).
[2] X. L. Qi and S. C. Zhang, Rev. Mod. Phys. **83**, 1057 (2011).
[3] N. P. Armitage, E. J. Mele, and A. Vishwanath, Rev. Mod. Phys. **90**, 015001 (2018).
[4] Y. Ando and L. Fu, Annu. Rev. Condens. Matter Phys. **6**, 361 (2015).
[5] M. Sato and Y. Ando, Rep. Prog. Phys. **80**, 076501 (2017).
[6] L. M. Schoop, M. N. Ali, C. Straßer, A. Topp, A. Varykhalov, D. Marchenko, V. Duppel, S. S. P. Parkin, B. V. Lotsch, and C. R. Ast, Nat. Commun. **7**, 11696 (2016).
[7] J. Hu, Z. Tang, J. Liu, X. Liu, Y. Zhu, D. Graf, K. Myhro, S. Tran, C. N. Lau, J. Wei, and Z. Q. Mao, Phys. Rev. Lett. **117**, 016602 (2016).
[8] R. Eppinga and G. Wiegers, Physica B+C **99**, 121 (1980).
[9] M. N. Ali, Q. D. Gibson, T. Klimczuk, and R. J. Cava, Phys. Rev. B **89**, 020505(R) (2014).
[10] G. Bian, T. R. Chang, R. Sankar, S. Y. Xu, H. Zheng, T. Neupert, C.-K. Chiu, S. M. Huang, G. Q. Chang, I. Belopolski, D. S. Sanchez, M. Neupane, N. Alidoust, C. Liu, B. K. Wang, C. C. Lee, H. T. Jeng, C. L. Zhang, Z. J. Yuan, S. Jia, A. Bansil, F. C. Chou, H. Lin, and M. Z. Hasan, Nat. Commun. **7**, 10556 (2016).
[11] C. L. Zhang, Z. J. Yuan, G. Bian, S. Y. Xu, X. Zhang, M. Z. Hasan, and S. Jia, Phys. Rev. B **93**, 054520 (2016).
[12] G. M. Pang, M. Smidman, L. X. Zhao, Y. F. Wang, Z. F. Weng, L. Q. Che, Y. Chen, X. Lu, G. F. Chen, and H. Q. Yuan, Phys. Rev. B **93**, 060506(R) (2016).
[13] M. X. Wang, Y. Xu, L. P. He, J. Zhang, X. C. Hong, P. L. Cai, Z. B. Wang, J. K. Dong, and S. Y. Li, Phys. Rev. B **93**, 020503(R) (2016).
[14] D. Shen, C. N. Kuo, T. W. Yang, I. Chen, C. Lue, and L. M. Wang, Commun. Mater. **1**, 56 (2020).
[15] E. Cheng, W. Xia, X. Shi, Z. Yu, L. Wang, L. Yan, D. C. Peets, C. Zhu, H. Su, Y. Zhang, D. Dai, X. Wang, Z. Zou, N. Yu, X. Kou, W. Yang, W. Zhao, Y. F. Guo, and S. Y. Li, npj Quantum Mater. **5**, 38 (2020).
[16] S. N. Guin, Q. Xu, N. Kumar, H. Kung, S. Dufresne, C. Le, P. Vir, M. Michiardi, T. Pedersen, S. Gorovikov, S. Zhdanovich, K. Manna, G. Auffermann, W. Schnelle, J. Gooth, C. Shekhar, A. Damascelli, Y. Sun, and C. Felser, Adv. Mater. **33**, 2006301 (2021).
[17] R. Sankar, G. N. Rao, I. P. Muthuselvam, T. R. Chang, H. T. Jeng, G. S. Murugan, W.-L. Lee, and F. C. Chou, J. Phys.: Condens. Matter. **29**, 095601 (2017).
[18] S.-Y. Guan, P.-J. Chen, M.-W. Chu, R. Sankar, F. C. Chou, H.-T. Jeng, C.-S. Chang, and T.-M. Chuang, Sci. Adv. **2**, e1600894 (2016).
[19] T. Le, Y. Sun, H. K. Jin, L. Che, L. Yin, J. Li, G. M. Pang, C. Q. Xu, L. X. Zhao, S. Kittaka, T. Sakakibara, K. Machida, R. Sankar, H. Q. Yuan, G. F. Chen, X. Xu, S. Li, Y. Zhou, and X. Lu, Sci. Bull. **65**, 1349 (2020).
[20] J. Wang, X. Xu, N. Zhou, L. Li, X. Cao, J. Yang, Y. Li, C. Cao, J. Dai, J. Zhang, Z. Shi, B. Chen, and Z. Yang, J. Supercond. Novel Magn. **28**, 3173 (2015).
[21] U. S. Kaluarachchi, Y. Deng, M. F. Besser, K. Sun, L. Zhou, M. C. Nguyen, Z. Yuan, C. Zhang, J. S. Schilling, M. J. Kramer, S. Jia, C. Z. Wang, K. M. Ho, P. C. Canfield, and S. L. Bud'ko, Phys. Rev. B **95**, 224508 (2017).
[22] C. Q. Xu, R. Sankar, W. Zhou, B. Li, Z. D. Han, B. Qian, J. H. Dai, H. Cui, A. F. Bangura, F. C. Chou, and X. Xu, Phys. Rev. B **96**, 064528 (2017).
[23] See Supplemental Material at http://link.aps.org/supplemental/10.1103/PhysRevB.106.L060501 for the experimental methods, sample characterizations, neutron scattering data, additional XRD data, and the resistivity data under pressure.
[24] X. Yang, J.-K. Bao, Z. Lou, P. Li, C. Jiang, J. Wang, T. Sun, Y. Liu, W. Guo, S. Ramakrishnan, S. R. Kotla, M. Tolkiehn, C.

Paulmann, G.-H. Cao, Y. Nie, W. Li, Y. Liu, S. van Smaalen, X. Lin, and Z.-A. Xu, Adv. Mater. **34**, 2108550 (2021).
[25] C. An, Y. H. Zhou, C. Chen, F. Fei, F. Q. Song, C. Park, J. Zhou, H.-G. Rubahn, V. V. Moshchalkov, X. Chen, G. Zhang, and Z. R. Yang, Adv. Mater. **32**, 2002352 (2020).
[26] C. L. Bull, N. P. Funnell, M. G. Tucker, S. Hull, D. J. Francis, and W. G. Marshall, High Press. Res. **36**, 493 (2016).
[27] B. H. Toby and R. B. V. Dreele, J. Appl. Crystallogr. **46**, 544 (2013).
[28] H. K. Mao, J. Xu, and P. M. Bell, J. Geophys. Res. **91**, 4673 (1986).
[29] O. Arnold, J. C. Bilheux, J. M. Borreguero, A. Buts, S. I. Campbell, L. Chapon, M. Doucet, N. Draper, R. Ferraz Leal, M. A. Gigg, V. E. Lynch, A. Markvardsen, D. J. Mikkelson, R. L. Mikkelson, R. Miller, K. Palmen, P. Parker, G. Passos, T. G. Perring, P. F. Peterson, S. Ren, M. A. Reuter, A. T. Savici, J. W. Taylor, R. J. Taylor, R. Tolchenov, W. Zhou, and J. Zikovsky, Nucl. Instrum. Methods Phys. Res. Sect. A **764**, 156 (2014).
[30] P. E. Blöchl, Phys. Rev. B **50**, 17953 (1994).
[31] G. Kresse and J. Furthmüller, Phys. Rev. B **54**, 11169 (1996).
[32] G. Kresse and D. Joubert, Phys. Rev. B **59**, 1758 (1999).
[33] J. P. Perdew, K. Burke, and M. Ernzerhof, Phys. Rev. Lett. **77**, 3865 (1996).
[34] A. F. Goncharov, Int. J. Spectrosc. **2012**, 617528 (2012).
[35] K. Kamali, T. R. Ravindran, and T. N. Sairam, Vib. Spectrosc. **71**, 12 (2014).
[36] M. R. Joya, J. Barba-Ortega, and P. S. Pizani, J. Appl. Phys. **113**, 013512 (2013).
[37] M. Pu, S. Liu, L. Lei, F. Zhang, L. Feng, L. Qi, and L. Zhang, Solid State Commun. **298**, 113645 (2019).
[38] E. Z. Kuchinskii, I. A. Nekrasov, and M. V. Sadovskii, J. Exp. Theor. Phys. **114**, 671 (2012).
[39] A. Glamazda, A. Sharafeev, R. Bohle, P. Lemmens, K. Y. Chou, and R. Sankar, Low Temp. Phys. **47**, 912 (2021).
[40] S. V. Ovsyannikov, N. V. Morozova, I. V. Korobeinikov, V. Haborets, R. Yevych, Y. Vysochanskii, and V. V. Shchennikov, Dalton Trans. **46**, 4245 (2017).
[41] https://www.cryst.ehu.es/rep/sam.html.
[42] P. Saha, B. Ghosh, A. Mazumder, K. Glazyrin, and G. D. Mukherjee, J. Appl. Phys. **128**, 085904 (2020).
[43] K. K. Mishra, T. R. Ravindran, J. O. Island, E. Flores, J. R. Ares, C. Sanchez, I. J. Ferrer, H. S. J. van der Zant, A. Pawbake, R. Kanawade, A. Castellanos-Gomez, and D. J. Late, ACS Appl. Nano Mater. **3**, 8794 (2020).
[44] M. M. Abd-Elmeguid, B. Ni, D. I. Khomskii, R. Pocha, D. Johrendt, X. Wang, and K. Syassen, Phys. Rev. Lett. **93**, 126403 (2004).
[45] T.-R. Chang, P.-J. Chen, G. Bian, S.-M. Huang, H. Zheng, T. Neupert, R. Sankar, S.-Y. Xu, I. Belopolski, G. Chang, B. K. Wang, F. Chou, A. Bansil, H.-T. Jeng, H. Lin, and M. Z. Hasan, Phys. Rev. B **93**, 245130 (2016).
[46] P.-J. Chen, T.-R. Chang, and H.-T. Jeng, Phys. Rev. B **94**, 165148 (2016).
[47] Z. M. Yu, Z. Zhang, G. B. Liu, W. Wu, X. P. Li, R.-W. Zhang, S. A. Yang, and Y. Yao, Sci. Bull. **67**, 375 (2022).
[48] W. Wu, Y. Liu, S. Li, C. Zhong, Z. M. Yu, X. L. Sheng, Y. X. Zhao, and S. A. Yang, Phys. Rev. B **97**, 115125 (2018).
[49] Z. Wang, Y. Sun, X. Q. Chen, C. Franchini, G. Xu, H. Weng, X. Dai, and Z. Fang, Phys. Rev. B **85**, 195320 (2012).
[50] B. J. Yang and N. Nagaosa, Nat. Commun. **5**, 4898 (2014).
[51] L. Fu and C. L. Kane, Phys. Rev. B **76**, 045302 (2007).
[52] S. Licciardello, J. Buhot, J. Lu, J. Ayres, S. Kasahara, Y. Matsuda, T. Shibauchi, and N. E. Hussey, Nature (London) **567**, 213 (2019).